Highlights

An adaptive multiscale quasicontinuum approach for mechanical simulations of elastoplastic periodic lattices

Li Chen,Péter Z. Berke,Thierry J. Massart,Stéphane P.A. Bordas,Lars A.A. Beex

- Elastoplastic periodic lattices are discretized using 3D beam finite elements.
- The generalized quasicontinuum method is applied for model reduction.
- A novel procedure for adaptive analysis is proposed to track evolving local plasticity.
- The method is validated by modeling scratching of a Kelvin lattice by a rigid sphere.
- The method is able to mechanically describe large scale lattices with accuracy and efficiency.

An adaptive multiscale quasicontinuum approach for mechanical simulations of elastoplastic periodic lattices

Li Chen[a,b,*], Péter Z. Berke[b], Thierry J. Massart[b], Stéphane P.A. Bordas[a] and Lars A.A. Beex[a]

[a]Faculty of Science, Technology and Medicine, Université du Luxembourg, 2 Av. de l'Universite, Esch-sur-Alzette, 4365, Luxembourg
[b]École polytechnique de Bruxelles, Université Libre de Bruxelles, Av. Adolphe Buyl 87, Ixelles, Brussels, 1000, Belgium

ARTICLE INFO

Keywords:
generalized quasicontinuum method
adaptivity
periodic lattice
elastoplasticity

ABSTRACT

The quasicontinuum method is a multiscale method that combines locally supported coarse-grained domains, with small regions in which the microstructural model is fully resolved. This contribution proposes the first adaptive formulation of the method for microstructural elastoplasticity. The microstructural model uses an elastoplastic beam description. The indicator for refinement is the occurrence of plastic deformation, such that plasticity can only occur in fully resolved regions. An illustrative numerical example of a scratch test of an elastoplastic Kelvin lattice demonstrates the capabilities of the resulting framework.

1. Introduction

Metallic periodic lattices have attracted more and more attention due to the progress in additive manufacturing and their outstanding mechanical properties (e.g. high strength-to-weight ratio, excellent energy absorption). Topologically, a periodic lattice is organized by repeating a unit cell in space. The unit cell consists of struts with a diameter that may desirably and/or undesirably vary along the struts' axial direction [12]. Experiments [5, 10] have attributed the failure of metallic periodic lattices to local nonlinear effects, such as elastic and plastic buckling of individual struts, which progress in plasticity and failure observable at the macroscale.

Particularly to study complex lattice mechanics of small and moderate sizes beam finite elements are used because of their computational efficiency, necessary for tackling multi millions strut problems. The main challenge of applying full beam descriptions to model lattice structures (referred to as direct numerical simulation or DNS) remains the associated prohibitive computational cost for engineering scale problems.

To simulate the nonlinear mechanical behavior of periodic lattices at the scale of products, model reduction is unavoidable. Thanks to the periodicity of lattices and the fact that localized straining/failure is often observed, concurrent multi-scale methods can be exploited. In particular, the quasicontinuum method (QC) is a potential solution because QC makes use of small fully-resolved domains (FRDs) to track localized deformation/failure, and computationally cheap coarse-grained domains (CGDs) in zones undergoing more homogeneous deformation. The work of [2, 13, 3, 4] extends the original QC (proposed for conservative atomic lattices) to simulate truss lattices (i.e. structural lattices) with dissipative mechanisms (e.g. elastoplasticity, damage). Until recently, the main bottleneck of this approach was that only a single FE (beam, spring) could be used to represent a strut. As a result, cross sections that fluctuate along the strut's axial direction could not be represented. This limitation was mitigated in [6], which generalized QC (the resulting method is termed as GQC) with a multi-field interpolation feature. Consequently, each strut can currently be more realistically modeled using a string of beam FEs with varying diameters.

Adaptivity (i.e. the evolution of the spatial reduction of the QC method based on the deformation) is crucial if the (local) deformation spatially evolves during the course of a simulation. In [7], Li et al. proposed an adaptive version of GQC (termed as AGQC), which exploits a novel refinement indicator to refine CGDs and transform CGDs into FRDs. It was proposed and critically assessed for elastic beams with geometrical nonlinearities. The capabilities and limitations of the refinement indicator for elastoplastic (geometrically nonlinear) beams have however not been investigated. In [15, 14], Rokoš et al. proposed an adaptive refinement strategy for QC to predict crack propagation in 2D lattice networks, in which each strut is represented using a truss element. Nevertheless, adaptive coarsening is considered as well. Mike et al. [9] applied QC with adaptive refinement for molecular statics simulations, where local atomic lattice behavior is confined to FRDs. Different refinement criteria were investigated. However, the refinement criteria (e.g. the local atom's site energy) are specific for atomistics and not applicable to beam lattices. Tembhekar et al. [16] proposed an adaptive refinement strategy for QC based atomistic simulations. The refinement indicator was chosen as the second principal invariant of the right Cauchy-Green tensor of CGDs. Phlipot et al. [11] applied similar adaptive refinement criterion for QC based beam lattice simulations. However, the adopted beams remained elastic. Moreover, the refinement indicator was chosen as the second principal invariants of the deformation gradients of CGDs, which triggers unnecessary refinement when CGDs are significantly but uniformly deformed.

*Corresponding author
li.chen@uni.lu (L. Chen); Peter.Berke@ulb.be (P.Z. Berke); Thierry.J.Massart@ulb.be (T.J. Massart); stephane.bordas@uni.lu (S.P.A. Bordas); lars.beex@uni.lu (L.A.A. Beex)
ORCID(s): 0000-0001-6351-9414 (P.Z. Berke); 0000-0001-7622-2193 (S.P.A. Bordas); 0000-0002-0486-6624 (L.A.A. Beex)

The main focus of present work is therefore the extension of the adaptive GQC (AGQC) framework of [7] towards elastoplasticity. This extension significantly widens the applicability of AGQC. Note that the present work (similar to [7]) only focuses on refinement and not on coarsening. To the best of the authors' knowledge, only [14] considered coarsening in QC frameworks.

The structure of this contribution is as follows: in Section 2, the key concepts of the AGQC are briefly revisited as to make the present work self-contained, while Section 3 briefly outlines the elastoplastic framework used for beams. In Section 4, the extension of the AGQC to elastoplastic lattices is presented. In Section 5, a numerical example is used to assess the proposed AGQC scheme. This is followed by conclusions drawn in Section 6, together with an outlook on future work.

2. Recap of the AGQC method

This section gives a brief recap of the generalized quasi-continuum method (GQC). A periodic lattice structure, the struts of which are discretized using beam FEs is considered and it is subjected to external forces. Let $\underline{u}$ and $\underline{f}_{\text{ext}}$ denote the column matrices storing the kinematic variables of the beam nodes and the corresponding external forces, respectively. Let $\underline{z}$ denote the column matrix that stores the plastic strain history variables of all beam FEs. The direct numerical simulation (DNS) of the lattice is incrementally performed by Newton's method for which the following system of linear equations must be solved for each iteration:

$$\delta\underline{u}^T(\underline{f}_{\text{int}}(\underline{u}^*,\underline{z}^*)+\underline{\underline{K}}(\underline{u}^*,\underline{z}^*)d\underline{u})=\delta\underline{u}^T\underline{f}_{\text{ext}} \tag{1}$$

where $\delta\underline{u}$ denotes the kinetically permissible virtual kinematic variables. $\underline{u}^*$ denotes the current estimate of $\underline{u}$, $d\underline{u}$ denotes the iterative correction of $\underline{u}$ and $\underline{z}^*$ denotes the current estimate of $\underline{z}$. Current estimate $\underline{z}^*$ (associated with current estimate $\underline{u}^*$) is calculated using a return mapping algorithm. $\underline{f}_{\text{int}}(\underline{u},\underline{z})$ denotes the column of internal forces and is obtained as:

$$\underline{f}_{\text{int}}(\underline{u},\underline{z})=\sum_{i=1}^{m}\int_{V_i}\underline{f}_i(\underline{u},\underline{z})dV \tag{2}$$

with m denoting the total number of beam FEs in the lattice and $\underline{f}_i$ the local force column of beam i. $\underline{\underline{K}}$ denotes the tangential stiffness matrix and is written as:

$$\underline{\underline{K}}(\underline{u},\underline{z})=\frac{\partial\underline{f}_{\text{int}}(\underline{u},\underline{z})}{\partial\underline{u}}=\sum_{i=1}^{m}\int_{V_i}\frac{\partial\underline{f}_i}{\partial\underline{u}}dV \tag{3}$$

The DNS is computationally too expensive to model large periodic lattices because of (1) the large number of DoFs involved; (2) the large number of beam FEs which need to be visited to construct Eq. (2) and Eq. (3) in Newton's incremental-iterative procedure. The GQC proposed in [6] mitigates the computational cost and maintains a satisfactory accuracy if local fluctuations only occur in the fully resolved domain. GQC performs model reduction in two steps, i.e. interpolation and summation.

Interpolation divides the lattice into fully-resolved domains (FRDs) and coarse-grained domains (CGDs). In the FRDs, all the kinematic variables of the beam nodes (i.e. displacements and rotations) are preserved. In the CGDs, a mesh of interpolation elements (IPEs) is introduced so that only a few representative kinematic variables are allocated to the IPE nodes. The kinematic variables of all beam nodes within an IPE are interpolated from their representative counterparts at the IPE nodes using FE shape functions. Moreover, the beam nodes are categorized into different groups based on periodicity. The IPE nodes store a set of representative kinematic variables for each type of beam node so as to interpolate the kinematic variables of each type of beam node independently. The only condition for this categorization of nodes is that the unit cell discretization is periodic. The reader is referred to [11] for details on how the categorization is performed.

Fig. 1 represents a lattice with a × shaped unit cell with a GQC spatial representation. After interpolation, the preserved kinematic variables (i.e. the displacements and rotations of the beam nodes in the FRDs and the representative displacements and rotations of all node types at the IPE nodes) are stored in a column matrix $\underline{u}_{\text{r}}$, which can be related to $\underline{u}$ via the interpolation matrix $\underline{\underline{N}}$ through

$$\underline{u}=\underline{\underline{N}}\,\underline{u}_{\text{r}}. \tag{4}$$

After interpolation, Eq. (1) is revised as

$$\delta\underline{u}_{\text{r}}^T(\underline{\underline{N}}^T\underline{f}_{\text{int}}(\underline{\underline{N}}\,\underline{u}_{\text{r}}^*,\underline{z}^*)+\underline{\underline{N}}^T\underline{\underline{K}}(\underline{\underline{N}}\,\underline{u}_{\text{r}}^*,\underline{z}^*)\underline{\underline{N}}d\underline{u}_{\text{r}})=\delta\underline{u}_{\text{r}}^T\underline{\underline{N}}^T\underline{f}_{\text{ext}} \tag{5}$$

with $\underline{u}_{\text{r}}^*$ denoting an estimate of $\underline{u}_{\text{r}}$ and $d\underline{u}_{\text{r}}$ the correction to $\underline{u}_{\text{r}}$.

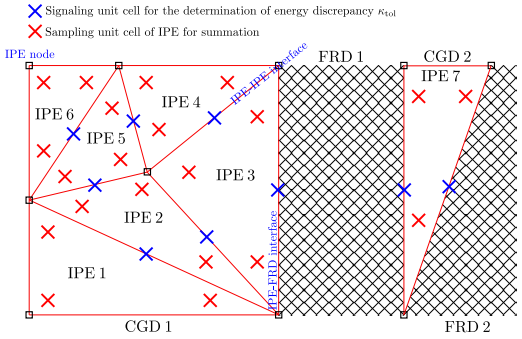

Figure 1: Illustration of key concepts of adaptive GQC method.

In summation, rather than visiting all beam FEs in the lattice according to Eqs. (2) and (3), only a selection of beam FEs are sampled to approximate $\underline{f}_{\text{int}}$ and $\underline{\underline{K}}$:

$$\bar{\underline{f}}_{\text{int}}(\underline{u}_{\text{s}},\underline{z}_{\text{s}})=\sum_{i\in S}\omega_i\int_{V_i}\underline{f}_i(\underline{u}_s,\underline{z}_s)dV \tag{6}$$

$$\bar{\underline{\underline{K}}}(\underline{u}_{\mathrm{s}}, \underline{z}_{\mathrm{s}}) = \frac{\partial \bar{\underline{f}}_{\mathrm{int}}(\underline{u}_{\mathrm{s}}, \underline{z}_{\mathrm{s}})}{\partial \underline{u}_{\mathrm{s}}} = \sum_{i \in S} \omega_i \int_{V_i} \frac{\partial \underline{f}_i}{\partial \underline{u}_s} dV \tag{7}$$

where S denotes the set of sampling beams, ω_i denotes the weight of sampling beam i, and $\underline{u}_{\mathrm{s}}$ the column matrix that stores the kinematic variables of the nodes of the sampling beams. $\underline{z}_{\mathrm{s}}$ represents the column matrix that stores the plastic strain history variables of all sampling beam FEs. Note that $\underline{u}_{\mathrm{s}}$ can be interpolated from $\underline{u}_{\mathrm{r}}$ using the interpolation matrix $\underline{\underline{N}}_{\mathrm{s}}$ through,

$$\underline{u}_{\mathrm{s}} = \underline{\underline{N}}_{\mathrm{s}} \underline{u}_{\mathrm{r}}. \tag{8}$$

The governing equations represented by Eq. (5) can then be further revised as

$$\delta \underline{u}_{\mathrm{r}}^T (\underline{\underline{N}}_{\mathrm{s}}^T \bar{\underline{f}}_{\mathrm{int}}(\underline{\underline{N}}_{\mathrm{s}} \underline{u}_{\mathrm{r}}^*, \underline{z}_{\mathrm{s}}^*) + \underline{\underline{N}}_{\mathrm{s}}^T \bar{\underline{\underline{K}}}(\underline{\underline{N}}_{\mathrm{s}} \underline{u}_{\mathrm{r}}^*, \underline{z}_{\mathrm{s}}^*) \underline{\underline{N}}_{\mathrm{s}} d\underline{u}_{\mathrm{r}}) = \delta \underline{u}_{\mathrm{r}}^T \underline{\underline{N}}^T \underline{f}_{\mathrm{ext}} \tag{9}$$

The reader is referred to [6] for details on how the sampling beams and their weights are selected.

In order to trace the evolution of localized deformation/failure, an adaptive GQC (AGQC) framework was proposed in [7] for elastic periodic lattices. The elastic AGQC monitors a sum of energy discrepancies, κ, at IPE-IPE interfaces and IPE-FRD interfaces using signalling unit cells (see Fig. 1). The calculation of κ is detailed in [7] and is not repeated here for the sake of brevity and focus. In short, a signalling unit cell is placed at the center of the interface between neighbouring IPEs or between the IPE and the FRD. The elastic strain energy of the signalling unit cell is evaluated using the IPE or FRD of both sides. The relative discrepancy of the elastic strain energy is defined as the energy discrepancy κ. Obviously, due to the presence of dissipation in elastoplasticity, the adaptive scheme can not apply to elastoplastic lattices in its original form. After each increment has converged, κ is evaluated for all signalling unit cells and compared to a user defined threshold, κ_{tol}. If the value of κ exceeds κ_{tol}, the associated IPEs are refined into smaller IPEs. If the volumes of the refined IPEs are smaller than a user defined volume threshold, V_{tol}, the associated IPEs are transformed into FRDs instead.

Either the refinement of IPEs or the transformation of IPEs into FRDs prompts the governing equations to be solved again for the current increment with the new GQC spatial representation in a so-called re-equilibration increment.

3. Elastoplastic beam description.

Each lattice strut is modeled using a string of elastoplastic 3D co-rotational beam FEs, for which plasticity is implemented here through cross sectional discretization and a multi-axial yield surface [1].

The 3D co-rotational framework elaborated in [6] decouples the overall beam motion (i.e. the nodal displacements and rotations at the beam ends in the global coordinate frame) into a rigid body movement (i.e. the displacements and rotations of the local coordinate frame) and a pure deformation (i.e. the displacements and rotations at the beam ends in the local coordinate frame).

The displacements and rotations at the beam ends in the local coordinate frame are then used to interpolate the normal and shear strains at each integration point of the central cross section. Afterwards, a return mapping algorithm is used to calculate the incremental plastic flow and the consistency condition with a von Mises yield criterion. Once the stress components and the tangential material stiffness of each integration point are obtained from the return mapping procedure, they are integrated to generate the internal forces and the consistent stiffness relationship. For more details of the formulation, readers are referred to [1].

The beam FE implementation [1] ensures a quadratic convergence rate in the implicit Newton scheme used in this work. A constant circular cross section is considered within a given element. To avoid shear locking for the beam FE, integration points are seeded in only one cross section (i.e. the central cross section). 100 quadrature points are used in the beam cross section at which the elastoplastic stress update takes place (See Fig. 2). For more details about the quadrature rules in a circular domain, readers are referred to [8].

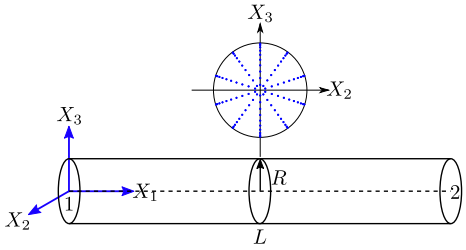

Figure 2: The integration scheme of the beam finite element. $\mathbf{X}_1$, $\mathbf{X}_2$, $\mathbf{X}_3$ span the local coordinate frame. Along the beam length direction, only the middle cross section is used for integration. In the central cross section, 100 quadrature points ($*$) are adopted.

4. AGQC method for elastoplasticity

This section upgrades the adaptive generalized quasicontinuum method of [7] so that elastoplastic lattice behaviour can be considered. The adaptive scheme is based on the refinement indicator of [7], complemented by a plastic flag. It is emphasized that in the new AGQC method, new sampling beams emerge when the spatial representation of GQC is adjusted in the refinement process. The newly introduced sampling beams emerge from (1) the sampling unit cells of the refined IPEs and (2) the IPEs that are transformed into FRDs.

Evaluating the internal forces and the tangential stiffnesses for these new sampling beams is required to solve the governing equations. In case of elastic behavior, the evaluation of the internal forces and the tangential stiffnesses

is independent of the deformation history. Consequently, in the elastic AGQC of [7], retrieving the internal forces and the tangential stiffnesses of new sampling beams is simple and performed in two steps: (1) interpolating their kinematic variables (i.e. the initial guess) and (2) re-equilibrating the unbalanced structural system. In case of elastoplasticity, the evaluation of the internal forces and the tangential stiffnesses depends on the plastic strains, that do not exist yet for newly introduced sampling beams.

This prompts two approaches to tackle plasticity in AGQC. The first is to allow plasticity in CGDs, in which case a carefully designed transfer of history variables is necessary. The second is to restrict plasticity to FRDs only, for which the transfer of history variables is circumvented and new sampling beams emerging from CGDs are presumed to be elastic before the re-equilibration step.

To assess the first approach, i.e. that allows plasticity in CGDs, the uniaxial compression of an elastoplastic body-centred cubic (BCC) lattice is considered first. Fig. 3 shows both the DNS and GQC results of a $12 \times 12 \times 12$ BCC lattice (comprising a volume of $24 \times 24 \times 24$ mm^3) under unconstrained uni-axial compression. Each of the 8 struts of a BCC unit cell is represented by three beam elements of equal length, among which diameters of 0.185 mm and 0.230 mm are chosen for beams in the center and at the ends. The material parameters in all simulations in the present work are: Young's modulus of 97 GPa, Poisson's ratio of 0.3, an initial yield stress of 325 MPa and a hardening modulus of 9.7 GPa (linear hardening is assumed). In the GQC simulation, the lattice is covered using 6 CGDs. The applied compressive engineering strain amounts to 20%.

The compression example in Fig. 3 shows that GQC can accurately capture the force–displacement curve, but fails to capture the deformation localization (Fig. 3b). When aiming at plastic CGD-to-FRD transformation involving the transfer of plastic strain history variables (one per cross sectional quadrature point) between sampling beams, significant convergence issues were observed. The lack of convergence is related to a failure of redistributing stresses from the homogeneously deformed plastic CGD pattern to a richer FRD representation. Such a redistribution is expected to result in strain localization with a pattern similar to the pure DNS, while respecting the requirement of the monotonous increase of the accumulated plastic strain history variable at each integration point.

The above could not be achieved without further development in the present framework which explains why we restrict plastic deformations to FRDs. An extension of the framework in which plasticity can develop in CGDs is planned as future work.

Plasticity is thus restricted in the present approach to FRDs only. Because plasticity should more often than not be treated as a localized phenomenon in metal lattices (see strain localization in Fig. 3b), this assumption corresponds well to the fundamental idea of classical QC utilizing FRDs to trace localized deformation/failure while limiting CGDs to sufficiently homogeneous elastic deformation modes. Under the assumption of restricting plasticity to FRDs, the adaptive scheme proposed in [7] was revised as Alg. 1 to account for elastoplasticity. The glossary of the symbols that are involved in Alg. 1 and its subroutine (i.e. Alg. 2) is given in Table 1.

Symbol	Description
t_k	The k^{th} time step in a Newton's scheme.
$\mathbf{\Omega}_k^{FRD}$	The FRDs at t_k.
$\partial\mathbf{\Omega}_k^{FRD}$	The boundary of the FRDs at t_k.
$\mathbf{\Omega}_k^{CGD}$	The CGDs at t_k.
$\partial\mathbf{\Omega}_k^{CGD}$	The boundary of the CGDs at t_k.
$\boldsymbol{\tau}_k$	The IPE & FRD configuration at t_k.
$\mathbf{S}^k$	The set of sampling beams at t_k.
$\underline{u}_r^k$	The reduced DoFs after interpolation at t_k.
$\underline{f}_{int}^k$	The internal force vector corresponding to $\underline{u}_r^k$.
$\underline{\underline{\Phi}}_k^{k-1}$	The interpolation matrix relating $\underline{u}_r^k$ to $\underline{u}_r^{k-1}$.
κ_{tol}	The threshold of the energy discrepancy.
V_{tol}	The minimally acceptable area/volume of a IPE.

Table 1
Glossary of the notations.

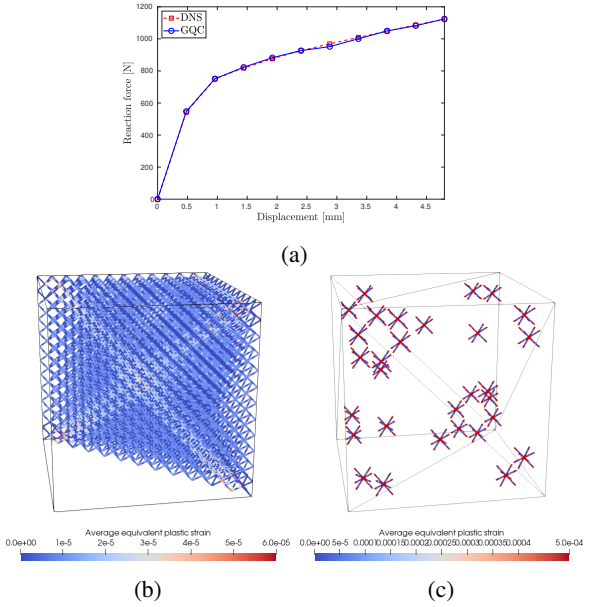

Figure 3: Unconstrained compression of a BCC lattice modeled using elastoplastic 3D co-rotational beam FEs. A non-homogeneous pattern of plastic straining develops in (the reference) DNS, which the CGD fails to capture. (a) Force–displacement curve, (b) Contour plot of averaged plastic strain in the beams in the DNS at a compression strain of 0.2, (c) Contour plot of averaged plastic strain of sampling beams in GQC at a compression strain of 0.2.

Alg. 1 starts from an initial division of FRDs (i.e. Ω_0^{FRD}) and CGDs (i.e. Ω_0^{CGD}), the initial mesh of IPEs in the CGDs (i.e. τ_0) and the initial selection of sampling beams (i.e. S^0).

For a given increment, t_k, the GQC model of the last converged increment, t_{k-1}, is preserved as the starting point (i.e. $\Omega_k^{\mathrm{FRD}} \Leftarrow \Omega_{k-1}^{\mathrm{FRD}}$, $\Omega_k^{\mathrm{CGD}} \Leftarrow \Omega_{k-1}^{\mathrm{CGD}}$, $\tau_k \Leftarrow \tau_{k-1}$ and $S^k \Leftarrow S^{k-1}$). Moreover, the kinematic variables and internal forces of the last converged increment (i.e. $\underline{u}_{\mathrm{r}}^{k-1}$ and $\underline{f}_{\mathrm{int}}^{k-1}$) serve as the initial guesses for their counterparts at t_k. The boundary conditions (BCs) at t_k (i.e. $\partial\Omega_k^{\mathrm{FRD}}$ and $\partial\Omega_k^{\mathrm{CGD}}$) are also imposed. The obtained GQC model is then solved for the equilibrium equations.

Once the GQC model is in equilibrium, it goes through three loops successively, i.e. Loop 1 (lines 6–10 in Alg. 1), Loop 2 (lines 11–15 in Alg. 1) and Loop 3 (lines 16–20 in Alg. 1). The three loops are identical, except for the different criteria that are applied to determine the target IPEs for refinement and for a difference in the refinement strategies. Loop 1 checks the sampling beams of all IPEs and targets the IPEs with plastified sampling beams for full resolution: IPEs flagged for plasticity are not refined but always transformed into FRDs. Loop 2 checks the energy discrepancy, κ for IPE-IPE interfaces and flags the IPEs with $\kappa > \kappa_{\mathrm{tol}}$ for refinement: IPEs are cut into smaller IPEs and the refined IPEs with smaller volumes than V_{tol} are transformed into FRDs. Loop 3 checks the energy discrepancy, κ, for IPE-FRD interfaces and flags the IPEs with $\kappa > \kappa_{\mathrm{tol}}$ for full resolution.

Either full resolution (Loop 1 & 3) or IPE refinement (Loop 2) generates a refined GQC model with a new division of FRDs ($\Omega_{k^*}^{\mathrm{FRD}}$) and CGDs ($\Omega_{k^*}^{\mathrm{CGD}}$), a new mesh of IPEs in CGDs (τ_{k^*}) and a new selection of sampling beams (S^{k^*}). This also creates new kinematic variables ($\underline{u}_{\mathrm{r}}^{k^*}$) and corresponding internal forces ($\underline{f}_{\mathrm{int}}^{k^*}$). Note that such a refined but not yet equilibrated GQC model at t_k is characterized by subscript/superscript k^* in order to distinguish it from the GQC model in equilibrium.

The just refined GQC model is generally no longer in equilibrium, and structural equilibrium needs to be found. First, the initial guesses of $\underline{u}_{\mathrm{r}}^{k^*}$ and $\underline{f}_{\mathrm{int}}^{k^*}$ are required. An interpolation matrix $\underline{\underline{\Phi}}_{k^*}^{k-1}$ between $\underline{u}_{\mathrm{r}}^{k-1}$ and $\underline{u}_{\mathrm{r}}^{k^*}$ is constructed (in the same manner as constructing $\underline{\underline{N}}$ in Eq. (4)) so that the initial guess of $\underline{u}_{\mathrm{r}}^{k^*}$ is set to $\underline{\underline{\Phi}}_{k^*}^{k-1}\,\underline{u}_{\mathrm{r}}^{k-1}$. To determine $\underline{f}_{\mathrm{int}}^{k^*}$ for this new initial guess, the history variables of the plastic sampling beams in S^{k-1} are transferred to their counterparts in S^{k^*}. It is worth noting that since only refinement is considered and plasticity is restricted to FRDs, FRDs can only grow in size and all sampling beams of FRDs in S^{k-1} are also sampling beams in S^{k^*}. This enables a straightforward transfer of history variables (see Fig. 4). Afterwards, the transferred history variables and the initial guess of $\underline{u}_{\mathrm{r}}^{k^*}$ are put into Eq. (6) to generate an initial guess for $\underline{f}_{\mathrm{int}}^{k^*}$.

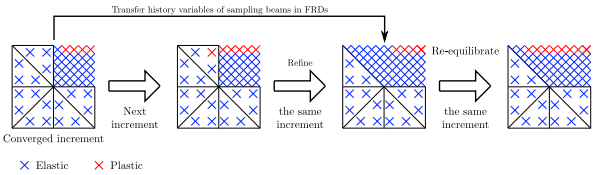

Figure 4: Illustration of transforming IPEs with plastic sampling beams into FRDs.

5. Numerical example

The elastoplastic AGQC is now illustrated by simulating the scratching of a Kelvin lattice using a rigid sphere. Each of the 36 struts in the Kelvin unit cell is discretized using single beam element. The categorization of node types (for the multi-field interpolation in the GQC approach)) and of beam types (for the purpose of evaluating κ) in the Kelvin unit cell are shown in Fig. 5.

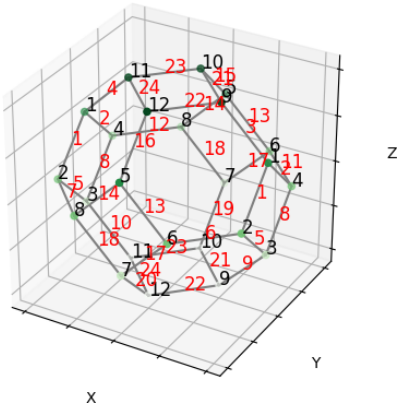

Figure 5: Beam representation of the Kelvin cell. Numbers in black and red are beam node types and beam element types, respectively.

Fig. 6 depicts the setup of the scratch simulation. The scratch depth is set to 0.1 l_{uc} (l_{uc} denotes the length of a unit cell, $l_{\mathrm{uc}} = 2$ mm). Only half of the lattice is considered thanks to the mirror plane symmetry. The contact between the rigid sphere and the beam FEs is frictionless and enforced using the penalty approach. The (horizontal) displacement increment of the rigid sphere is set to 1.5 l_{uc} and an automatic refinement of the increment is performed in case of divergence of the Newton's scheme. The DNS includes 738,800 beam FEs and 2,272,800 DoFs and is not computed due to computational limitations.

The initial setup of the AGQC model is shown in Fig. 7. An FRD of $10 \times 10 \times 10$ unit cells is located near the initial position of the rigid sphere. The rest of the domain is a CGD with a structured mesh of linear tetrahedral IPEs. 5 quadrature points (i.e. sampling unit cells) are adopted in each IPE.

5.1. Choice of control parameters of AGQC

Two control parameters (κ_{tol} and V_{tol}) need to be chosen by the user for the AGQC simulation. κ_{tol} is the threshold for

Algorithm 1: Adaptive scheme. The difference with Alg. 2 of [7] is indicated in italic (steps 6-10).

1 Initialization prior to simulation: configure GQC model (Ω_0^{FRD}, Ω_0^{CGD}, τ_0, S^0), $\underline{u}_{\mathrm{r}}^0 = \mathbf{0}$, $\underline{f}_{\mathrm{int}}^0 = \mathbf{0}$.
2 **for** k = 1,2,...,n **do**
3 Inherit GQC model ($\Omega_k^{\mathrm{FRD}} \Leftarrow \Omega_{k-1}^{\mathrm{FRD}}$, $\Omega_k^{\mathrm{CGD}} \Leftarrow \Omega_{k-1}^{\mathrm{CGD}}$, $\tau_k \Leftarrow \tau_{k-1}$, $S^k \Leftarrow S^{k-1}$), set initial guesses $\underline{u}_{\mathrm{r}}^k \Leftarrow \underline{u}_{\mathrm{r}}^{k-1}$, $\underline{f}_{\mathrm{int}}^k \Leftarrow \underline{f}_{\mathrm{int}}^{k-1}$.
4 Apply boundary conditions at t_k.
5 Equilibrate the GQC model.
6 *Identify the IPEs with plastic sampling beams and collect them in set $\tau_{resolve}$.*
7 **while** $\tau_{\mathrm{resolve}} \neq \emptyset$ **do**
8 *Fully resolve IPEs in $\tau_{resolve}$.*
9 *Invoke subroutine in Alg. 2.*
10 *Identify the IPEs with plastic sampling beams and collect them in set $\tau_{resolve}$.*
11 Evaluate energy discrepancy (κ) for IPE-IPE interfaces in $\boldsymbol{\tau}_{\mathrm{k}}$, identify the IPEs with $\kappa > \kappa_{\mathrm{tol}}$ and collect them in set $\boldsymbol{\tau}_{\mathrm{refine}}$.
12 **while** $\boldsymbol{\tau}_{\mathrm{refine}} \neq \emptyset$ **do**
13 Invoke refinement algorithm in Alg. 1 of [7].
14 Invoke subroutine in Alg. 2.
15 Evaluate energy discrepancy (κ) for IPE-IPE interfaces in $\boldsymbol{\tau}_{\mathrm{k}}$, identify the IPEs with $\kappa > \kappa_{\mathrm{tol}}$ and collect them in set $\boldsymbol{\tau}_{\mathrm{refine}}$.
16 Evaluate energy discrepancy κ for IPE-FRD interfaces in $\boldsymbol{\tau}_{\mathrm{k}}$, identify the IPEs with $\kappa > \kappa_{\mathrm{tol}}$ and collect them in set $\boldsymbol{\tau}_{\mathrm{resolve}}$.
17 **while** $\boldsymbol{\tau}_{\mathrm{resolve}} \neq \emptyset$ **do**
18 Fully resolve IPEs in τ_{resolve}.
19 Invoke subroutine in Alg. 2.
20 Evaluate energy discrepancy (κ) for IPE-FRD interfaces in $\boldsymbol{\tau}_{\mathrm{k}}$, identify the IPEs with $\kappa > \kappa_{\mathrm{tol}}$ and collect them in set $\boldsymbol{\tau}_{\mathrm{resolve}}$.
21 Store output data of current time step: Ω_k^{FRD}, Ω_k^{CGD}, τ_k, S^k, $\underline{u}_{\mathrm{r}}^k$, $\underline{f}_{\mathrm{int}}^k$.

Algorithm 2: Subroutine of structural re-equilibration.

Input: Refined but not equilibrated GQC model ($\Omega_{k^*}^{\mathrm{FRD}}$, $\Omega_{k^*}^{\mathrm{CGD}}$, τ_{k^*}, S^{k^*}, $\underline{u}_{\mathrm{r}}^{k^*}$, $\underline{f}_{\mathrm{int}}^{k^*}$).
Input: GQC model of the last converged (equilibrated) increment ($\Omega_{k-1}^{\mathrm{FRD}}$, $\Omega_{k-1}^{\mathrm{CGD}}$, τ_{k-1}, S^{k-1}, $\underline{u}_{\mathrm{r}}^{k-1}$, $\underline{f}_{\mathrm{int}}^{k-1}$).
Output: Equilibrated GQC model (Ω_k^{FRD}, Ω_k^{CGD}, τ_k, S^k, $\underline{u}_{\mathrm{r}}^k$, $\underline{f}_{\mathrm{int}}^k$).
1 Compute interpolation matrix $\underline{\underline{\Phi}}_{k^*}^{k-1}$ between $\underline{u}_{\mathrm{r}}^{k^*}$ and $\underline{u}_{\mathrm{r}}^{k-1}$. Set the initial guess of $\underline{u}_{\mathrm{r}}^{k^*}$ to be $\underline{\underline{\Phi}}_{k^*}^{k-1}\, \underline{u}_{\mathrm{r}}^{k-1}$.
2 Transfer history variables of plastic sampling beams in S^{k-1} to their counterparts in S^k.
3 Set the initial guess for $\underline{f}_{\mathrm{int}}^{k^*}$ by solving Eq. (6).
4 Equilibrate the GQC model.

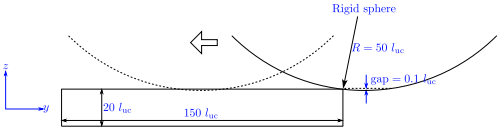

(a) 2D view.

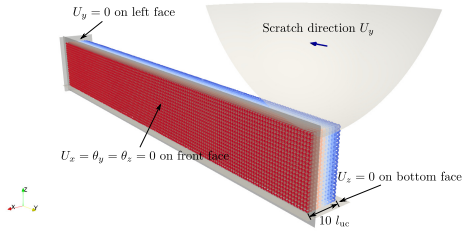

(b) 3D view.

Figure 6: Setup for scratching with a rigid sphere.

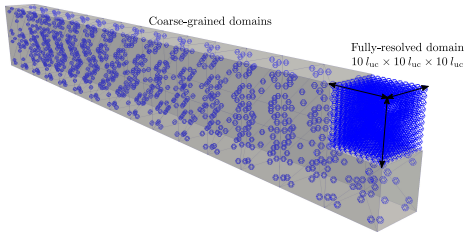

Figure 7: Initial AGQC model for the scratch test. Sampling unit cells are shown in blue.

the energy discrepancy for IPE-IPE and IPE-FRD interfaces. V_{tol} is the threshold below which an IPE is fully resolved. Following the results of [7], V_{tol} is set to $10l_{\mathrm{uc}}^3$ in this study.

To choose κ_{tol}, the 1st increment (during which contact is established) of the AGQC model of Fig. 7 is computed. The resulting energy discrepancies of the IPE-IPE and IPE-FRD interfaces at the beginning of the simulation are sorted, from

which three different candidate values for κ_{tol} (0.15, 0.25 and 0.35) are chosen heuristically.

The CGDs and FRDs after refinement in the first increment are shown in Fig. 8. As expected, a smaller value for κ_{tol} results in more refinement and takes more time to complete. the first increment with $\kappa_{\text{tol}} = 0.35$ is approximately 2.7 times faster than that with $\kappa_{\text{tol}} = 0.15$ and the first increment with $\kappa_{\text{tol}} = 0.25$ is approximately 1.5 times faster than that with $\kappa_{\text{tol}} = 0.15$.

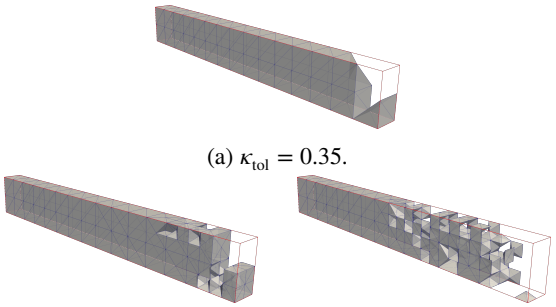

(a) $\kappa_{\text{tol}} = 0.35$.

(b) $\kappa_{\text{tol}} = 0.25$. (c) $\kappa_{\text{tol}} = 0.15$.

Figure 8: IPEs after the 1st increment for different values for κ_{tol}. Voids represent FRDs.

Fig. 9 shows the evolution of the normal contact force F_z as function of κ_{tol} for the 1st increment (relative to the value for $\kappa_{\text{tol}} = 0.15$), together with the fractions of the number of DoFs (relative to the DNS), of the number of sampling beams (relative to the DNS) and of the CGD's volume (relative to the entire volume) . F_z is used as an indicator of the overall structural response. Smaller values for κ_{tol} yield more accurate simulations, but compromise the model reduction as it (most notably) increases the sizes of the FRDs.

As the vertical contact force hardly changes for the considered values for κ_{tol}, 0.35 is chosen as the optimal value to maximise the computational efficiency. However, since the DNS result is not available as reference, $\kappa_{\text{tol}} = 0.25$ is also computed for comparison purposes.

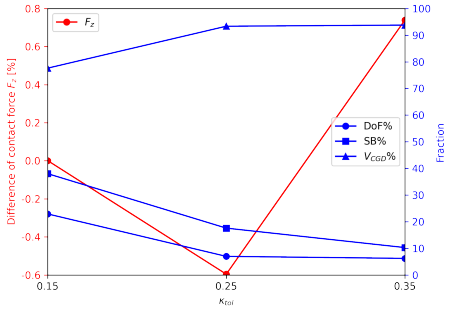

Figure 9: Fractions of: F_z (relative to F_z of $\kappa_{\text{tol}} = 0.15$), of the number of DoFs (relative to the DNS), of the number of sampling beams (relative to the DNS) and of the CGD's volume (relative to the entire volume) as functions of κ_{tol} after refinement of the 1st increment.

5.2. Results

The evolution of the IPEs and FRDs, of the total deformation and of the plastic strains in the scratch test are presented in Fig. 10. The images clearly show that the scratching induces strain localization below the rigid sphere. The plastic strain zone only reaches a depth of a few unit cells, whereas the induced displacement fluctuation below the sphere reaches much larger depth.

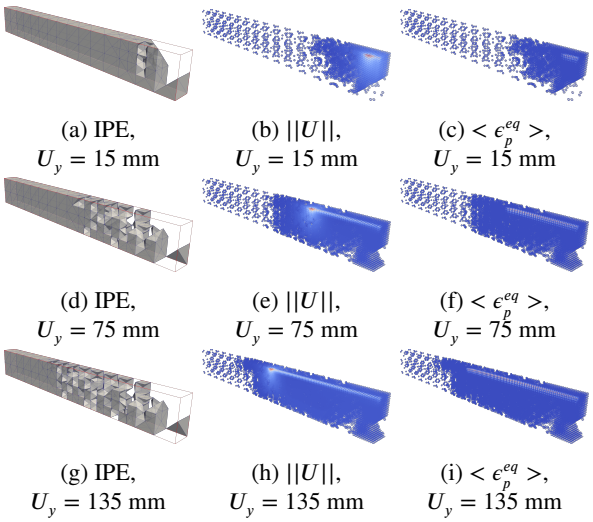

(a) IPE, $U_y = 15$ mm (b) $||U||$, $U_y = 15$ mm (c) $< \epsilon_p^{eq} >$, $U_y = 15$ mm

(d) IPE, $U_y = 75$ mm (e) $||U||$, $U_y = 75$ mm (f) $< \epsilon_p^{eq} >$, $U_y = 75$ mm

(g) IPE, $U_y = 135$ mm (h) $||U||$, $U_y = 135$ mm (i) $< \epsilon_p^{eq} >$, $U_y = 135$ mm

Figure 10: AGQC results for $\kappa_{\text{tol}} = 0.35$ as a function of the displacement of the rigid sphere (U_y). Left column: IPEs. Central column: displacement magnitude of the nodes of the sampling beams. The color ranges from 0 mm (blue) to 1.8 mm (red). Right column: average cumulative strains $< \epsilon_p^{eq} >$ in the sampling beams. The color ranges from 0 (blue) to 0.019 (red).

The evolving IPEs and FRDs in the left column of Fig. 10 clearly show the capacity of the proposed AGQC to adapt the model in the elastoplastic domain. The reasons for refinement are analyzed in details later.

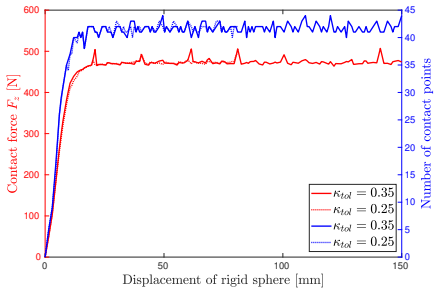

Figure 11: The vertical contact force F_z and the number of contact points as a function of the displacement of the rigid sphere. Only a displacement of up to 81 mm is considered for $\kappa_{\text{tol}} = 0.25$.

The vertical contact force versus the (horizontal) displacement of the rigid sphere is presented in Fig. 11, together with the number of active contact points. A comparison of the vertical and horizontal contact forces is shown in Fig. 12.

In Fig. 11, the number of active contact points fluctuates. This is caused by the discrete nature of the lattice, as beams establish and lose contact with the sphere during the sphere's horizontal movement. Note that the results for $\kappa_{\text{tol}} = 0.35$ and $\kappa_{\text{tol}} = 0.25$ are quite similar, showing that $\kappa_{\text{tol}} = 0.35$ leads to sufficiently accurate results. Synchronized periodic spikes can be observed for both F_y and F_z in Fig. 12. A logical explanation is that the periodicity of the force response is caused by the periodicity of the lattice, coupled to the mechanism of contact–no contact oscillations. Note furthermore that F_x is not presented in Fig. 12 as it is zero due to symmetry. The fact that F_y is non-zero is completely due to plasticity; if an elastic lattice would be considered, the value for F_y would only be non-zero at the start of the scratch test.

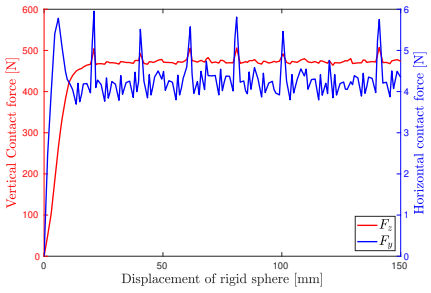

Figure 12: The vertical and horizontal contact forces as a function of the displacement of the rigid sphere for $\kappa_{\text{tol}} = 0.35$.

Fig. 13 depicts the progressive refinement of AGQC using the percentages of the number of DoFs, of the number of sampling beams and of the volume of the CGD. Throughout the simulation, more than 70% of the lattice remains coarse grained with $\kappa_{\text{tol}} = 0.35$. The number of sampling beams remains less than 50% of the DNS and the number of DoFs never exceeds 30% of the DNS. This constitutes a significant computational saving and demonstrates the efficiency of the proposed formulation. The AGQC model for $\kappa_{\text{tol}} = 0.25$ is more refined compared to that of $\kappa_{\text{tol}} = 0.35$ because the percentages of the number of DoFs, of the number of sampling beams and of the volume of the CGDs become larger. Almost identical force–displacement curves are obtained for $\kappa_{\text{tol}} = 0.35$ and $\kappa_{\text{tol}} = 0.25$, yet $\kappa_{\text{tol}} = 0.25$ leads to a substantially larger FRD volume fraction and hence, less computational saving.

Fig. 14 shows the number of refinement iterations during the course of the simulation. The total number of refinement iterations per increment is broken down into the refinement iterations that occur in Loop 1 (refinement to forbid plasticity occurring in IPEs, lines 6–10 in Alg. 1), Loop 2 (refinement because κ_{tol} is exceeded at IPE-IPE interfaces, lines 11–15 in Alg. 1) and Loop 3 (refinement because κ_{tol} is exceeded at IPE-FRD interfaces, lines 16–20 in Alg. 1). Fig. 14 shows that Loop 1 is a necessary enhancement to the refinement criterion of [7] if plasticity is to be restricted to FRDs. Refinement because κ_{tol} is exceeded at IPE-IPE interfaces occurs more often than refinement at IPE-FRD interfaces. The latter, however, seems to occur more regularly. The refinement triggered by plasticity occurring in IPEs starts when the displacement of the rigid sphere reaches 20 mm and occurs regularly afterwards.

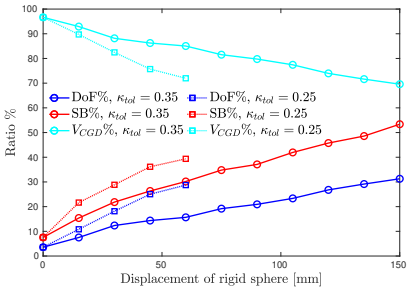

Figure 13: The percentages of the number of DoFs (relative to the DNS), of the number of sampling beams (relative to the DNS) and of the CGD's volume (relative to the entire volume) as a function of the displacement of the rigid sphere. Only a displacement of up to 81 mm is considered for $\kappa_{\text{tol}} = 0.25$.

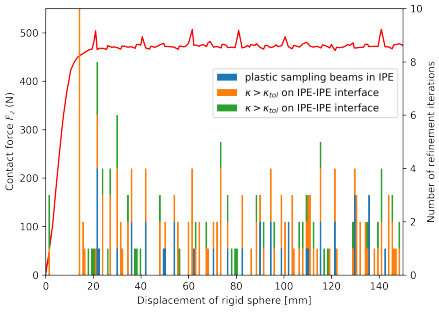

Figure 14: Vertical contact force F_z and the refinement iterations as functions of the scratch displacement for $\kappa_{\text{tol}} = 0.35$.

This computational example shows that the enhanced AGQC method is a powerful numerical tool to study the elastoplastic behavior of large structural lattices as it significantly reduces the model size in terms of the number of DoFs and the number of sampling beams. More computational savings are expected for models in which localization occurs in smaller regions relative to the entire modelling domain. Vice versa, if localization (e.g. long shear bands) appears throughout larger parts of the domain, less computational saving can be expected.

6. Conclusion and outlook

An extension of a previously proposed adaptive generalized quasicontinuum method (AGQC) for elastic lattices is presented to account for elastoplastic material behavior in periodic lattices with plasticity restricted to the fully-resolved domains. In the new scheme, all the sampling beams of interpolation elements in an AGQC model are monitored for plastic deformation. If any sampling beam

of an interpolation element undergoes plastic deformation, the interpolation element is transformed into a fully resolved domain. Such an arrangement simplifies the transfer of history variables of sampling beams in the GQC models. Because the history variables may only be non-zero in the sampling beams of fully-resolved domains and the size of the fully-resolved domains monotonically increases, a plastic sampling beam of a fully-resolved domain in the unrefined GQC model remains a sampling beam in the fully-resolved domain in the refined GQC model, for which the history variable can be directly inherited.

The enhanced AGQC was applied to study the behavior of an elastoplastic Kelvin lattice scratched by a rigid sphere. It was shown that the lattice behavior can be simulated at a substantially lower computational effort than the direct numerical simulation (DNS) thanks to the adaptive refinement.

In future work, rather than restricting plasticity to the fully-resolved domains (FRDs), the possibility of incorporating plasticity in the coarse-grained domains (CGDs) and the CGD-to-FRD transformation are planned to be further investigated. The coarsening of the elastoplastic AGQC model may also be investigated in order to further boost the computational efficiency of the AGQC method.

7. Acknowledgement

The authors gratefully acknowledge the support of Fonds National de la Recherche of Luxembourg, Grant/Award Number: FNRS-FNR grant INTER/FNRS/15/11019432/EnLight-enIt/; Grant/Award Number: BRIDGES/2019/MS/14-31062-4/ROPETEST/; Fonds De La Recherche Scientifique - FNRS of Belgium, Grant/Award Number: Grant PDR No. 26033553 (EnLightenIt).

References

[1] J. Battini et al. Plastic instability of beam structures using co-rotational elements. Comput. Methods Appl. Mech. Eng., 191(51):5811 – 5831, 2002.

[2] L. Beex et al. A multiscale quasicontinuum method for dissipative lattice models and discrete networks. J. Mech. Phys. Solids, 64:154 – 169, 2014.

[3] L. Beex et al. Quasicontinuum-based multiscale approaches for plate-like beam lattices experiencing in-plane and out-of-plane deformation. Comput. Methods Appl. Mech. Eng., 279:348 – 378, 2014.

[4] L. Beex et al. Higher-order quasicontinuum methods for elastic and dissipative lattice models: uniaxial deformation and pure bending. GAMM-Mitt., 38(2):344–368, 2015.

[5] H. Carlton et al. Mapping local deformation behavior in single cell metal lattice structures. Acta Mater., 129:239 – 250, 2017.

[6] L. Chen et al. Generalized quasicontinuum modeling of metallic lattices with geometrical and material nonlinearity and variability. Comput. Methods Appl. Mech. Eng., 366:112878, 2020.

[7] L. Chen et al. A refinement indicator for adaptive quasicontinuum approaches for structural lattices. Int. J. Numer. Methods Eng., 122(10):2498–2527, 2021.

[8] A. Mazzia et al. Product gauss quadrature rules vs. cubature rules in the meshless local petrov–galerkin method. J. Complexity, 26(1):82 – 101, 2010.

[9] K. Mikeš, O. Rokoš, and R. H. J. Peerlings. Molecular statics simulation of nanoindentation using adaptive quasicontinuum method. In Acta Polytechnica CTU Proceedings, volume 15. Czech Technical University in Prague, 2018.

[10] R. Mines. Some Fundamental Structural Ideas for Conventional Metallic Lattice Structures, pages 7–15. Springer International Publishing, Cham, 2019.

[11] G. P. Phlipot and D. M. Kochmann. A quasicontinuum theory for the nonlinear mechanical response of general periodic truss lattices. Journal of the Mechanics and Physics of Solids, 124:758 – 780, 2019.

[12] C. Portela et al. Impact of node geometry on the effective stiffness of non-slender three-dimensional truss lattice architectures. Extreme Mech. Lett., 22:138 – 148, 2018.

[13] O. Rokoš et al. A variational formulation of dissipative quasicontinuum methods. Int. J. Solids Struct., 102-103:214 – 229, 2016.

[14] O. Rokoš, R. H. J. Peerlings, and J. Zeman. eXtended variational quasicontinuum methodology for lattice networks with damage and crack propagation. Computer Methods in Applied Mechanics and Engineering, 320:769 – 792, 2017.

[15] O. Rokoš, R. H. J. Peerlings, J. Zeman, and L. A. A. Beex. An adaptive variational quasicontinuum methodology for lattice networks with localized damage. International Journal for Numerical Methods in Engineering, 112(2):174–200, 2017.

[16] I. Tembhekar, J. S. Amelang, L. Munk, and D. M. Kochmann. Automatic adaptivity in the fully nonlocal quasicontinuum method for coarse-grained atomistic simulations. International Journal for Numerical Methods in Engineering, 110(9):878–900, 2017.